A β–spectrometer for searching effects of finite neutrino masses

E. Holzschuh W. Kündig L. Palermo H. Stüssi P. Wenk

Physik-Institut der Universität Zürich, CH-8057 Zürich, Switzerland

EXT-2000-123
23/12/1998

Abstract

A detailed description of a Tret'yakov-type magnetic β–spectrometer with electrostatic acceleration is presented. The instrument is being used for high precision measurements of the β–spectra of various isotopes and to search for neutrino mixing and heavy neutrinos with masses up to $100\,\mathrm{keV}/c^2$. The relative momentum resolution, obtained with an extended source ($3 \times 2\,\mathrm{cm}^2$) and a large silicon strip detector, is $\delta p/p = 6.9 \times 10^{-4}$ (FWHM). The width of the energy band, which can simultaneously be measured with this resolution, is typically 50 times larger than the corresponding width of the energy resolution. The detector delivers pulse-height and one-dimensional position information. The read-out electronics provides a seperate channel for each detector strip, allowing measurements to be made with high count rate and small dead-time losses. The detection of scattered electrons was minimized by the arrangement of baffles and by the use of materials with small atomic number. Experimentally, scattering in the spectrometer was investigated by accelerating photoelectrons up to 60 keV energy. A system for measuring the corresponding high voltage is described. Extensive Monte Carlo simulations of scattering in the spectrometer have been performed. Good agreement with the experimental data was obtained and there was no need to adjust any scattering cross section to the particular experimental situation. We conclude that calculated scattering probabilities can reliably be used in the analysis of experimental β–spectra, which is important as otherwise scattering would constitute a major uncertainty.

Key words: Neutrino masses; β–spectroscopy; Monte Carlo simulation
PACS: 14.60.Pq, 29.30.Dn, 34.50Bw

1 Introduction

In this article we present a magnetic spectrometer, designed for high precision measurements of the shape of β–spectra. The instrument was built to search for effects of neutrino masses and mixing.

For zero neutrino masses, a β–spectrum is expected to be smooth and structureless. The hypothesis to be tested assumes that the electron antineutrino emitted in β–decay is actually a mixture of several states with masses m_i . If true, β–decay could be a multichannel process, where each decay branch is characterized by a mass m_i and a branching fraction. Specifically, it may be that there is a state with a negligibly small mass m_1 and a second state with a much larger mass m_2 . In this case, a discontinuity in slope [1] (a "kink") is expected if m_2c^2 is smaller than the spectrum endpoint energy E_0.

No particular assumptions about the nature of the state with mass m_2 must be made. It may be the dominant part of one of the known neutrinos, the muon or the tau neutrino, or it may be a sofar unknown sterile neutrino. Searches may be made with any β–decay. Hence, isotopes to be used may be chosen for experimental convenience.

In practice, m_2 must be relatively large, i.e. much larger than the mass limit of order $10\,\mathrm{eV}/c^2$ found in recent experiments concentrating on the endpoint region of the tritium β–spectrum [2–6]. For m_2 above about $1\,\mathrm{keV}/c^2$, β–spectroscopy should be sensitive for a branching fraction of about 10^{-3} or even less. We note that experiments of this type have been performed before, but mostly for the ill fated 17 keV neutrino (for a review see Ref. [7]). A systematic search over a large mass range has not been reported so far.

Neutrino oscillation experiments are sensitive to effects of much smaller neutrino masses, but in principle can measure only differences of the squared masses (for a general review see [8]). In practice, small mixing can only be detected with the so-called appearance mode, excluding e.g. sterile neutrinos. Hence the two types of experiments, neutrino oscillation and β–spectroscopy, explore different regions of a large parameter space.

The kink-like structure in an otherwise smooth β–spectrum provides a unique signature for neutrino mixing, provided the spectrum is measured with sufficient energy resolution. Good resolution and at the same time high count rate can be achieved with magnetic spectrometers. The instrument presented here is of the Tret'yakov type [9]. This type was developed by Tret'yakov from the old orange-type spectrometer but it is much simpler since it requires only straight current conductors. This makes it relatively easy to built a large device with high mechanical precision. As a consequence Tret'yakov-type spectrometers were used in a number of recent tritium experiments [2,3,5]. Details of our design are described in Sec. 2.

By using a position-sensitive detector in the focal plane of the spectrometer, it is possible to measure simultaneously an energy band which is much wider than the width of the resolution. We are using a large silicon strip detector. The detector and the associated electronics are described in Sec.s 2.6–7. Each

detector strip is connected to an independent electronic channel making it possible to measure with high count rates and with small dead-time losses.

Traditionally, β–spectra were recorded by varying the electric current of the magnet. For this measuring mode, the width of a momentum band as determined by apertures and by the detector geometry, is strictly proportional to the magnetic field strength and therefore to the current in an iron-free spectrometer. This advantage is offset by the fact that the spectrum shape is directly affected by any energy-dependent detection efficiency. We therefore use another mode of measurement in which decay electrons are electrostatically accelerated. The magnet current is kept constant and a negative high voltage, applied to the β–source, is varied. Electrons arriving at a certain detector position have constant energy, making the shape of a measured spectrum independent of any detection efficiency. The price to be paid for this advantage is that the solid angle, accepted by the spectrometer at the source, becomes a function of the acceleration voltage. The required correction must be calculated. We give a simple formula for our geometry and show by Monte Carlo simulation that it accurately describes the correction up to moderately high acceleration voltages. The electron-optical properties of the spectrometer are described in Sec. 3.

Scattering from baffle edges, current conductors and other spectrometer structures causes electrons to be detected with grossly wrong energies. This leads to long-range distortions in a measured β–spectrum. Such distortions are smooth functions of energy and cannot mimic a kink as expected from neutrino mixing. For the analysis of a β–spectrum, a good quantitative knowledge is nevertheless important. The detection of scattered electrons was minimized by the design, but for the present spectrometer type it cannot be avoided completely. In Sec. 4 we present results of extended Monte Carlo simulations and compare them with measurements made with accelerated photoelectrons.

2 Spectrometer

2.1 Overview

The spectrometer was designed for a maximum electron energy of 200 keV and a relative energy resolution of approximately $\delta E/E \simeq 10^{-3}$ full width at half maximum (FWHM). It is obvious that one wants to use strong sources for high count rates. A source however must also be very thin to keep the energy loss of electrons passing throught the source layer small. Therefore it should be possible to use extended sources without compromizing the spectrometer resolution. The count rate can be further incresed by a large detector with

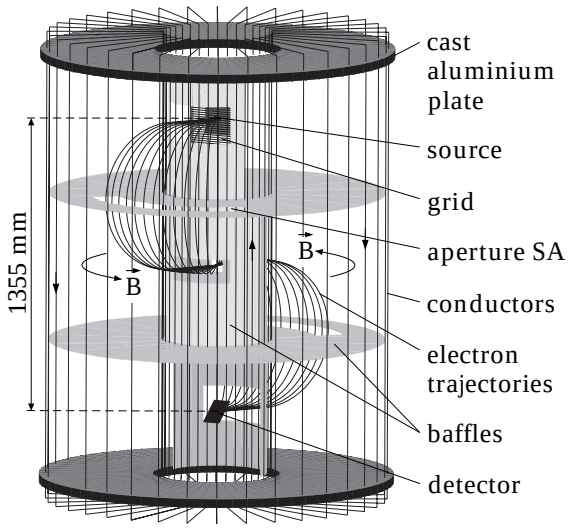

Fig. 1. Simplified view of the spectrometer.

position resolution.

A simplified overview of the spectrometer is shown in Fig. 1. The main component is a set of $n = 72$ rectangular current loops forming a toroidal magnetic field. Electrons from the source are transported in two 180° bends to the detector. There is one intermediate, approximate focus which is not useful for spectroscopy, but a baffle at this position is quite efficient for blocking scattered electrons.

A convenient feature of this arrangement is that the magnetic field can be accurately calculated by analytical methods. Using cylindrical coordinates, the contribution from the inner ring of conductors with current I is given by

$$\begin{aligned} B_\rho &= \frac{\mu_0}{2\pi}\frac{nI}{\rho}\,\frac{q\sin(n\varphi)}{1+q^2-2q\cos(n\varphi)} \\ B_\varphi &= -\frac{\mu_0}{2\pi}\frac{nI}{\rho}\,\frac{q^2-q\cos(n\varphi)}{1+q^2-2q\cos(n\varphi)} \end{aligned} \tag{1}$$

where

$$q := (\rho/R_1)^n \tag{2}$$

and where R_1 is the radial distance of the conductors. Similar equations, with opposite sign, hold for the outer ring of conductors at a radial distance R_2. In the space of possible electron trajectories, the contribution of the outer conductors as well as the contribution of the radial conductors are negligible. For radial distances $\rho < R_1$, the field drops very quickly to zero. Within the torus ($R_1 = 250\,\mathrm{mm}$, $R_2 = 780\,\mathrm{mm}$), the field is approximately the same as of

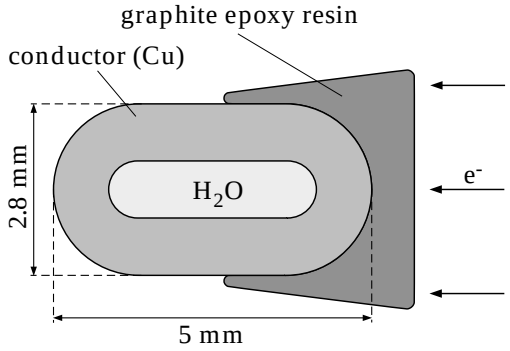

Fig. 2. Cross section of the current conductors at places where they can be hit by electrons.

a single wire on the spectrometer axis,

$$B_\varphi \simeq -\frac{\mu_0}{2\pi}\frac{nI}{\rho}\,, \quad R_1 + h < \rho < R_2 - h\,, \tag{3}$$

carrying a current nI. This approximation is valid, provided the quantity h in Eq. (3) is taken to be somewhat larger than the distance between adjacent conductors.

2.2 Spectrometer details

The current conductors were fabricated from Cu tubing with an outer diameter of 8 mm for the inner ring and 10 mm for the outer ring conductors. To allow for thermal expansion, the conductors are guided at one end with spring-loaded clamps. Deformations due to magnetic forces are avoided by holding the conductors under strong tension and by guides in the two horizontal baffle planes (Fig. 1), fixing the conductor positions in azimuthal directions.

At positions, where the electron trajectories pass through the inner ring of conductors, thin conductor segments with an oval cross section were inserted to improve the transmission. This is shown in Fig. 2. The thin segments were fitted with epoxy shields as discussed below.

The 72 current loops must be interconnected for a complete electric circuit, which was done at radius 490 mm at the upper radial conductors. The connections are equivalent to an unwanted circular current producing a large stray magnetic field. This field is compensated by two circular conductors, just below and above the radial conductors, carrying the spectrometer current in equal parts. The arrangement is shown in Fig. 3. For the same reason, the current supply is connected to the spectrometer by a coaxial feed-through and cable. The output of the current supply is symmetrically grounded by two resistors

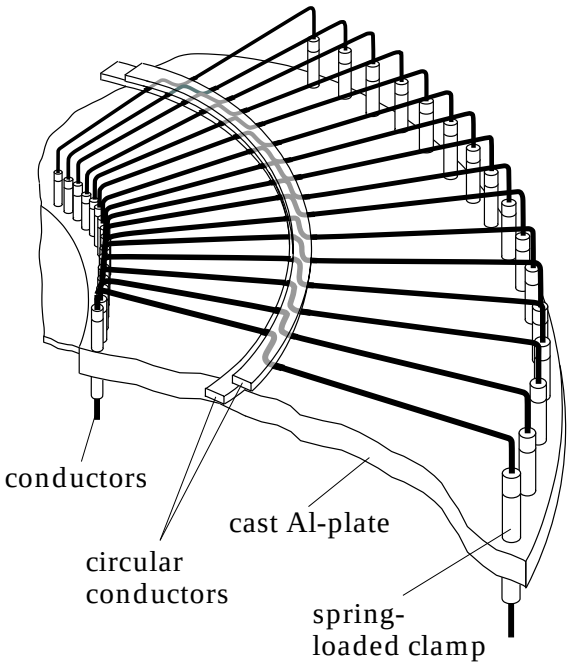

Fig. 3. Part of the upper radial conductors and compensation of the loop connections.

and the electric potential of the current loops is at most $\pm 20\,\mathrm{V}$ with respect to ground. The resulting stray electric fields are considered negligible.

At a maximum current of $I = 150\,\mathrm{A}$, the power dissipated in the spectrometer is about 6 kW. The cooling system to remove this heat load consists of a heat exchanger and a closed water circuit with circulating pump and deionizer. The water temperature is stabilized by a feedback loop. The water flow through the current conductors is divided into 14 parallel segments, i.e. the paths of the electric current and the water flow are not the same. During operation, part of the circulating water flows continuously through the deionizer, resulting in a water resistivity of typically $10\,\mathrm{M\Omega\,cm}$. The resulting leakage currents, bypassing the current loops through the water, are less than $1\,\mu\mathrm{A}$ and thus negligible.

The earth's magnetic field is compensated by three sets of large square coils, approximately forming a cube with 5 m edge length. The field is measured with a three-axis magnetometer and the coil currents are controlled by three feedback loops. Over the volume of the spectrometer, the residual field is 1 mG or less. This is negligible compared with a typical spectrometer field of 30 G (at $\rho = 500\,\mathrm{mm}$) necessary to focus electrons with an energy of 100 keV.

The system of baffles was designed such that an electron backscattered from any baffle surface needs at least to be scattered a second time to reach the detector. As shown in Fig. 1 and with more details in Fig. 4, there are two horizontal baffle planes and a set of cylindrically shaped baffles. In addition, there

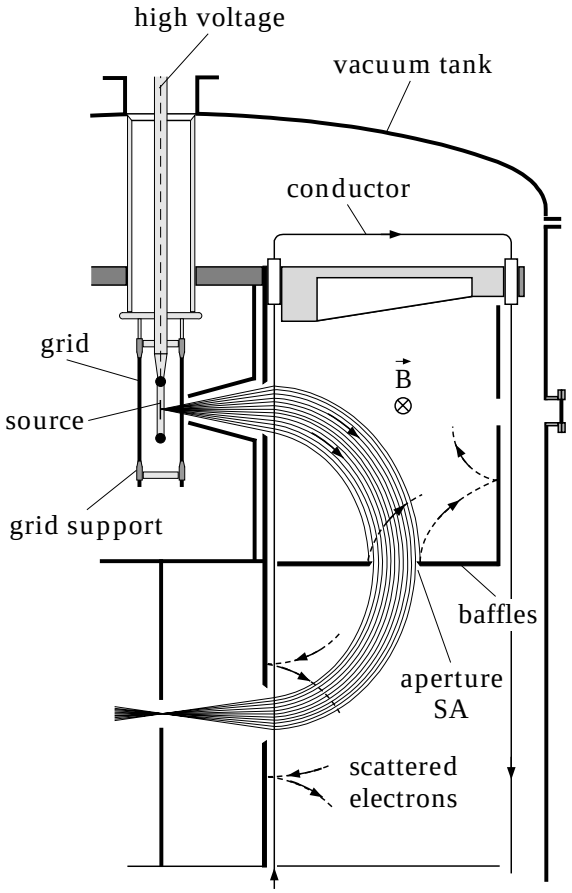

Fig. 4. Source region and details of the arrangement of baffles.

are vertical baffles (not shown) oriented radially which block any scattered electrons outside the channel of normal trajectories.

The opening of the first baffle plane (SA) defines the solid angle accepted by the spectrometer. All other openings were chosen such that an electron, passing SA with the necessary momentum to reach the detector, will also pass all other openings with certainty.

The baffles were made of aluminium. To minimize backscattering, their surfaces were painted with graphite, i.e. a material with small atomic number. The thickness of the layer, approximately 0.1 mm, was chosen such that an electron, penetrating the graphite and being backscattered from the aluminium, loses so much energy that it can not be detected. Similarly, the current conductors, at places where electron trajectories pass through the inner ring of conductors, were fitted with shields, the cross section being shown in Fig. 2. The shields were made of a material with small atomic number. An epoxy resin was used, with graphite powder added to avoid electrostatic charging and to match more closely the thermal expansion coefficient of copper. The shields were given a shape such that scattering in the forward direction is avoided. For the same reason, all contours of the baffle apertures were beveled.

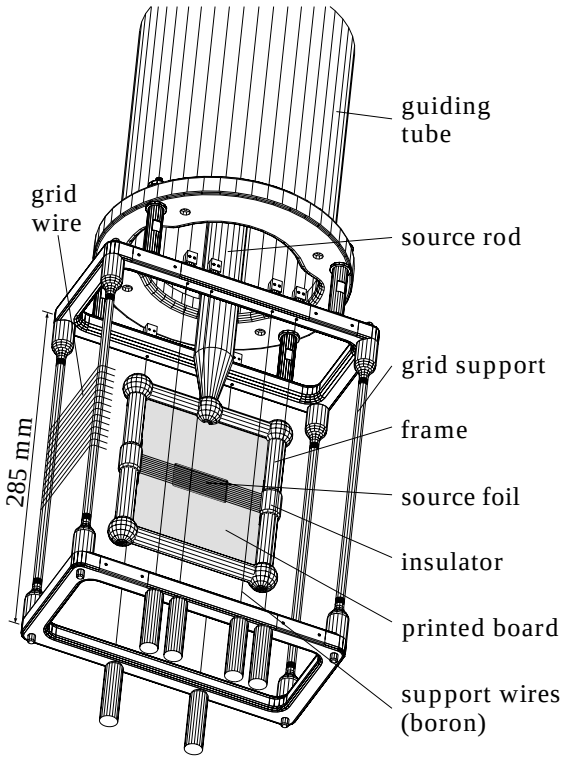

Fig. 5. Source assembly, high voltage connection and grid. For clarity, only a small fraction of the grid wires is shown.

2.3 Source assembly and grid

The spectrometer allows the use of extended sources (up to $2 \times 4\,\mathrm{cm}^2$) with good energy resolution. The source holder (see Fig. 5) consists of a frame of copper tubes and a copper coated board. The tubes are held together by copper spheres (20 mm diameter) suitable for the required high voltage.

The frame is supported by a long (1.8 m) isolated rod which serves also as a feed-through for the high voltage. The rod consists of a plexiglas tube (30 mm diameter) and an inner copper tube which allows electrical connections. The space between the tubes was filled (bubble-free) with a silicone resin (Dow Corning, Sylgard 184). Several rods of this type were made and tested with voltages up to 100 kV, without any problems.

The source holder is surrounded by a box-like grid (Fig. 5). The grid was made with bonding wire (Al - Si(2%) alloy) having a 17.5 μm diameter and a 1 mm spacing between the wires. The optical transmission of the grid is 98.25 %. To prevent significant deformation of the grid due to electrostatic forces, the grid is supported by boron fibers (142 μm diameter) loaded with a tension of 15 N.

Stray electric fields outside the grid can be avoided by putting the grid on a certain potential V_{grid} with a sign opposite to the potential, V_{S} , of the source

holder. Assuming the source plane and the grid can be extended to infinity (perpendicular to the plane of Fig. 4), a valid approximation for the limited space with electron trajectories reaching the detector, this electrostatic problem can be solved analytically. We find

$$V_{\mathrm{grid}} = V_{\mathrm{S}} \, \frac{b}{2\pi d} \ln \frac{2\pi r}{b} \,, \tag{4}$$

where $2r$ is the wire diameter ($17.5\,\mu$m), b is the wire spacing (1 mm) and where d is the distance between the source plane and the grid (50 mm).

2.4 Solid angle correction

The solid angle, accepted by the spectrometer at the source for $V_{\mathrm{S}} = 0$, is determined by the aperture SA (see Figs. 1 and 4). The limiting angles at the source are $\varphi_{\max} = \pm 25^{\circ}$ in azimuthal direction and $\theta_{\max} = \pm 5^{\circ}$ for the angle of elevation with respect to the horizontal plane. For $V_{\mathrm{S}} < 0$, the electrons are bent towards the direction of the electric field and the solid angle increases with increasing source voltage. Assuming the electric field to be homogeneous, the direction after acceleration can be determined for any given direction at the source by using conservation of energy and of the momentum component perpendicular to the electric field. Assuming further that the accepted angles are as small as given above and that the aperture SA is far away, the solid angle at the source can be calculated. With these approximations, valid for our case, we find for the correction of the solid angle

$$S(V_{\mathrm{S}}) = \frac{Z}{\varphi} \, \arcsin(Z \sin \varphi) \,, \tag{5}$$

where

$$Z := p_{\mathrm{mag}}/p \tag{6}$$

is the ratio of the spectrometer momentum setting and the momentum at the source, and where the normalization $S(0) = 1$ is chosen. This formula is remarkable in several respects. It is independent of the distance between source and grid, to first order it is independent of the small angle $\theta_{\max}$ and finally for small acceleration, $S \simeq Z^2$ is in leading order independent of all geometry factors. In reality, the situation is more complicated. Due to the blocking of trajectories by the current conductors, the solid angle is cut into many small pieces and the angle φ in Eq. (5) is not identical with $\varphi_{\max}$ but smaller. We will come back to this point in Sec. 3.1 where we present Monte Carlo simulations.

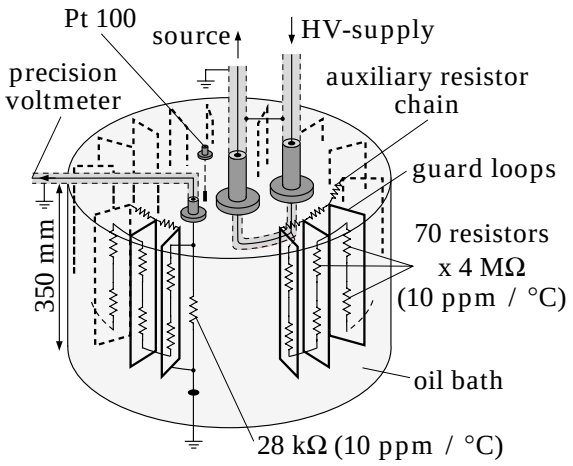

Fig. 6. High voltage divider in an oil bath and with guards to avoid large local electric fields. The temperature is measured with a platinum resistor (Pt 100).

2.5 Source voltage system

The spectrometer allows the use of extended sources, provided their vertical extension is compensated electrostatically. This is achieved by dividing the source into many conducting strips (width typically 1 mm) and by choosing a strip potential which is a linear function of the strip position with respect to the source centre. Hence these potentials or gradient voltages can be simply generated by a resistor chain with equal resistors. The source strips are indicated in Fig. 5. The resistors are on the source board inside the frame.

The complete source voltage system consists of a high voltage supply (FUG, 70 kV), a precision high voltage divider, a precision voltmeter (Schlumberger Solartron 7081) and the gradient supplies.

The gradient supplies are operated on high voltage. Two of them are required to generate voltages (up to ± 1500 V) which are symmetric with respect to the potential of the source centre. These supplies are powered by solar cells illuminated by a metal halide lamp.

A schematic view of the high voltage divider is shown in Fig. 6. Wire-wound precision resistors with a specified temperature coefficient of 10 ppm are used. The divider is formed by 70 resistors, 4 MΩ each, and a 28 kΩ resistor connected to the voltmeter. The resistors are mounted in a tank filled with a dust-free and dehydrated oil.

Special measures were taken to avoid large local electric fields at the resistors or their connections. In particular, the resistors are surrounded by a cage of rectangular-shaped metal loops, arranged in the form of two thirds of a torus. A chain of auxiliary resistors from voltage input to ground connects the loops.

The geometry is such that locally the potential of a loop and an adjacent measuring resistor is approximately equal.

There are several advantages using such a cage. Small leakage currents between high voltage and ground are unavoidable, even with high quality oil. With the chosen arrangement, such currents flow mainly from the cage to ground, putting a small additional load on the supply but not affecting the measured voltage. The cage can be given a shape, which is well suited for high voltage and sharp edges with large electric fields are avoided.

The divider was tested with voltages up to 70 kV and no indications for high voltage instabilities were observed. Calibration to better than 10^{-4} was achieved by comparison with another high voltage divider (up to 20 kV) from an earlier experiment [3].

2.6 Detector

A silicon strip detector is used, consisting of four silicon plates with a sensitive area of $8.0 \times 3.05\,\mathrm{cm}^2$ each and the total detector area is thus $97.6\,\mathrm{cm}^2$. There are 24 strips on each plate with 1.27 mm pitch. This rather wide pitch was chosen to be just compatible with the spectrometer resolution and to minimize the total number of electronic read-out channels (total 96) required.

The detector plates were produced out of high resistivity n-type silicon wafers. The strips are p^+ implants of boron with 1 mm width and are metallized with a $1\,\mu$m layer of aluminium. Each plate is surrounded by a set of ten narrow guard rings. The backplane is an n^+ implant of phosphorus.

Two batches of detector plates have been produced, the thickness of the wafers being $370\,\mu$m in the first and $300\,\mu$m in the second batch. The plates from the first batch showed rather large leakage currents, typically 150 nA per strip at 22° C. The second batch turned out to be much better, the leakage currents being in the range $4-9$ nA per strip for selected plates. The backplane of these plates was metallized with a $0.1\,\mu$m layer of aluminium for better electric contacts. The performance data given in the following refer to the second batch.

The silicon plates are mounted on ceramic carriers as illustrated in Fig. 7. The detector is operated in vacuum and some cooling is required. Sufficient thermal coupling between silicon plate and carrier was achieved by the electrical contacts from the detector strips to the signal leads on the carrier using 1 mm wide strips cut from $25\,\mu$m thick high purity aluminium foil.

At the nominal operating temperature of 0° C, the bias voltage for full deple-

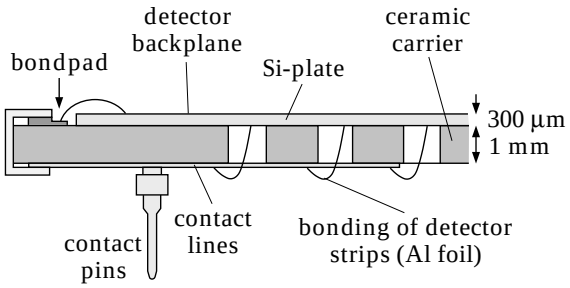

Fig. 7. Mounting of the silicon detector on a ceramic carrier.

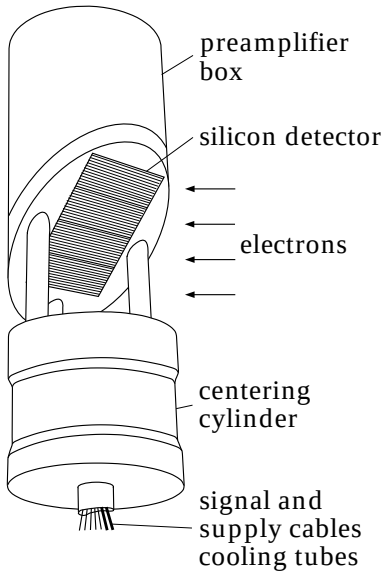

Fig. 8. Mounting of the silicon strip detector.

tion of the detector is 45 V and the average leakage current is 1.5 nA per strip. The total capacitance of one strip was measured to be 40 pF. From this value, 2×2 pF can be attributed to coupling to the neighbouring strips.

The complete detector assembly is shown in Fig. 8. The detector plates are located in the focal plane of the spectrometer, making an angle $\theta_{\mathrm{D}} = 48.5°$ with respect to the spectrometer axis. The value of θ_{D} was determined by optimizing the spectrometer resolution with Monte Carlo simulation (see Sec. 3). Electrons, incident form the right, hit the detector backplane which is held at ground potential.

One-dimensional position is simply determined by the strip number, i.e. the full resolution is 1.27 mm. The preamplifiers are located in the box just above the detector plates. Signal cables and other connections are fed through the support tubes as indicated. The detector is cooled by circulating a cold liquid through the base of the preamplifier box. Thermal coupling to the detector plates is made by the electrical contacts through vacuum-tight feed-throughs.

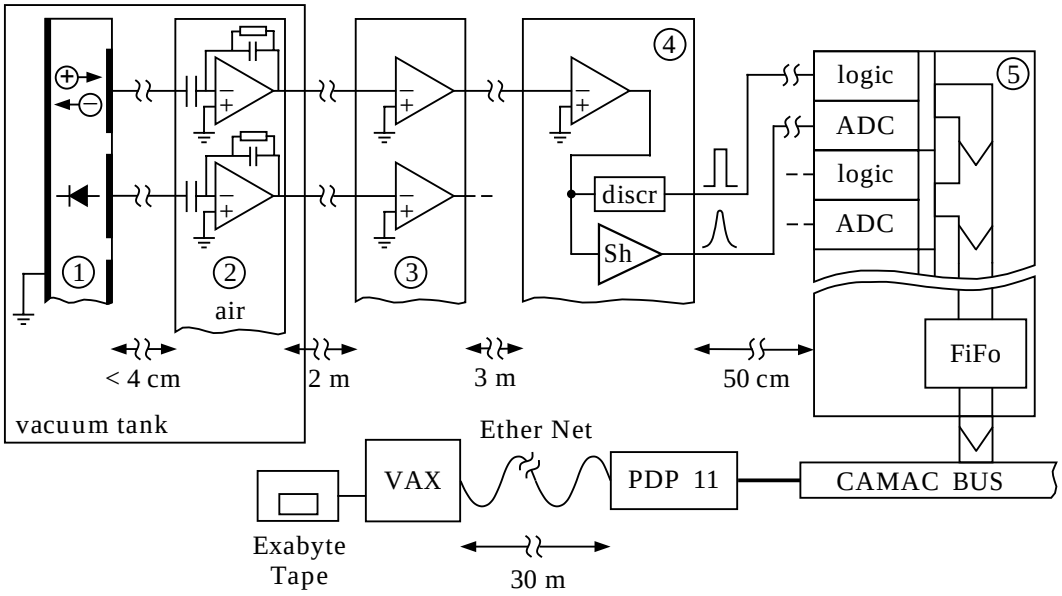

Fig. 9. Simplified block diagram of the detector read-out electronics.

2.7 Electronics

Each detector strip (out of 96) is read out by a separate electronic channel. A simplified block diagram is shown in Fig. 9. The preamplifiers (LeCroy HQV820M) (2) are AC-coupled to the detector (1) and have a time constant of 200 μs. The preamplifier signals are brought out of the spectrometer by mini-coaxial cables and are amplified by a factor 100 using fast amplifiers (3) to avoid problems with electromagnetic interference.

The main amplifiers (4) are of conventional design, producing approximate gaussian output pulses with a fixed time constant of 1 μs. Four amplifiers and discriminators are housed in one NIM module. The discriminators serve as triggers and their threshold is normally set just above the noise level.

Analog to digital conversion (5) is triggered by the discriminators. The main building blocks for one channel are a linear peak-stretcher, a successive approximation ADC (LTC 1272) and some control logic. Eight channels are built into one double-width CAMAC module.

There is also logic which detects coincidences between neighbouring channels. This allows one to identify electrons hitting the detector close to the borderline of two strips. In such cases, the charge produced in the detector may be divided and collected by two strips. Double counting can be avoided by combining such events or by rejecting both.

A 16 bit data word is formed from the ADC outputs (11 bits), from two coincidence bits, and from three bits identifying the channel number within

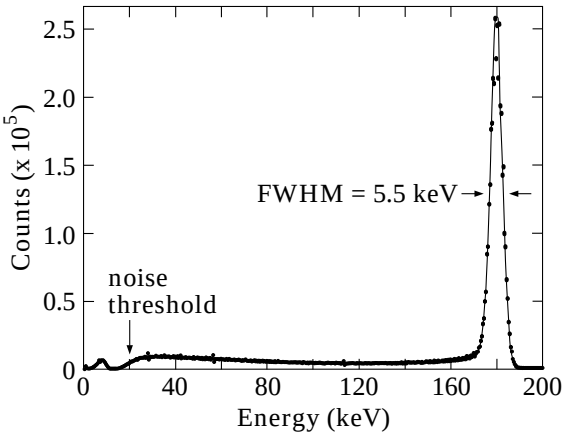

Fig. 10. Typical pulse-height distribution from one detector strip for 180 keV electrons.

one module. These data are transfered via a 16 bit wide bus into a FiFo memory (SN74ACT7808) with 2048 word depth for temporary storage. There is only one FiFo per module as the transfer time into the FiFo is much smaller than the ADC conversion time (5 μs).

The data are read from the FiFo memory by a front-end computer (PDP11-72) via a CAMAC bus and transmitted through an Ethernet link for further processing and final storage.

The width of the pulse-height resolution achieved with this system is 5.5 keV FWHM with the detector cooled to 0°C. Figure 10 shows the pulse-height distribution from one detector strip hit by 180 keV electrons. The extended tail is due to electrons which are backscattered from the detector and deposit only part of their energy in the silicon. The fraction of events in the tail is 36(1)%, determined by the fact that on the average the electron trajectories make an angle of 48.5° with respect to the detector normal.

It should be noted that the pulse-height information is only used for applying cuts in the off-line analysis and for monitoring detector performance and stability of the electronic gain. For these purposes successive approximation ADC's are quite sufficient.

3 Optical properties

We define the optical properties to be the spectrometer properties if electron scattering is neglected. These properties are energy resolution, dispersion, accepted solid angle etc., and are determined by the configuration of electric and magnetic fields, the arrangement of baffles, and the size of source and detector.

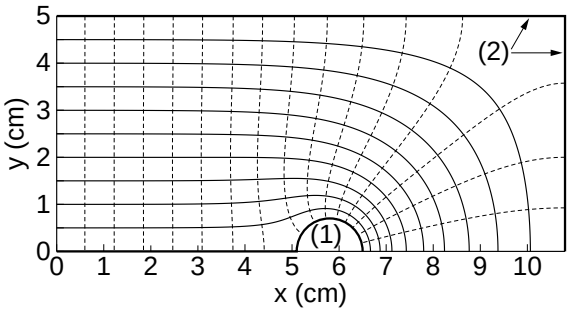

Fig. 11. Contour lines of constant electric potential (solid) and electric field lines (dashed) between source holder (1) at a voltage V_S and grounded grid (2).

3.1 Simulation

The computations were performed in a straight forward way by numerically solving the equation of motion using a fifth-order Runge-Kutta algorithm with automatic step-size adjustment [10]. Initial conditions were generated to simulate a flat and extended source with uniform surface activity emitting electrons isotropically. The magnetic field was computed using Eq. (1).

The electric field between source holder and grid is to a first approximation homogeneous in the region where trajectories are accepted by the spectrometer. To test this, the field was computed numerically using a fourth-order difference method for the two-dimensional Laplace equation. The field inhomogeneity due to the finite spacing of the grid (1 mm) was negleted by replacing the grid by grounded planes. The result is plotted in Fig. 11. Only one quadrant is shown because of symmetry. The source is located at $y = 0$ and extends to typically $|x| \leq 15\,\mathrm{mm}$. Trajectories accepted by the spectrometer cross the grid at $y = 50\,\mathrm{mm}$ in a typical range $|x| \leq 40\,\mathrm{mm}$ for moderately high fields. The electric field in this region deviates from uniformity by approximately 1%.

The gradient voltage at the source (Sec. 2.5) is determined by the energy dispersion of the spectrometer. The latter is conveniently expressed by the momentum dispersion

$$\frac{dp}{dz} = p/\lambda \tag{7}$$

where z is the coordinate along the spectrometer axis and λ is a length constant, characteristic of the spectrometer. Using relativistic kinematics, the energy dispersion follows

$$D_E := \frac{dE}{dz} = \frac{E}{\lambda}\,\frac{E + 2m_e c^2}{E + m_e c^2}\,. \tag{8}$$

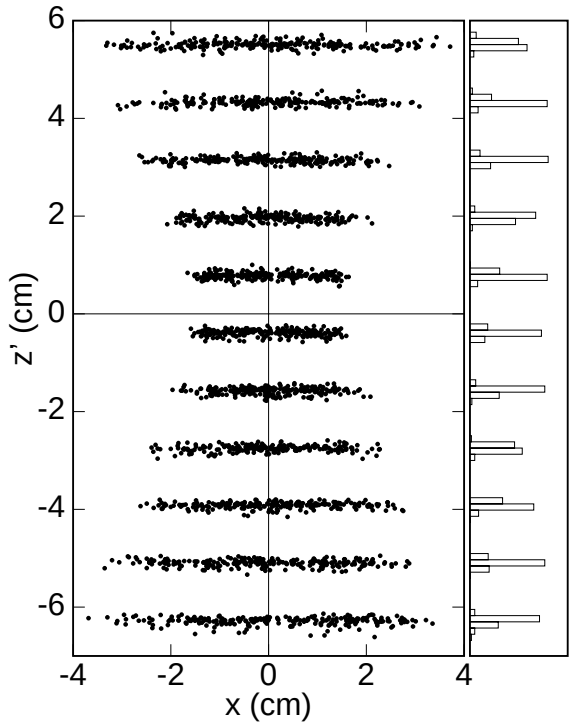

Fig. 12. Plane of the detector with some electron hits marked. The histogram on the right was obtained by projecting the events on the z'–axis. (See text).

The gradient voltage between adjacent source strips is now determined by the condition

$$\delta V_{\mathrm{grad}} = aD_E/e\,, \tag{9}$$

where a is the strip pitch and e is the magnitude of the electron charge. In the simulations, V_{grad} was taken into account by requiring energy conservation, i.e. the deformation of the electric field configuration was neglected. This is justified, because the electron energies considered are much larger than eV_{grad}. From the simulations we find $\lambda = 2182\,\mathrm{mm}$.

The focusing properties of the spectrometer are illustrated in Fig. 12, showing the detector plane with some electron hits. The source was assumed to have a size of $3 \times 2\,\mathrm{cm}^2$ emitting monoenergetic electrons. The magnet setting was taken to be constant and the source voltage V_{S} was varied in equal steps. Each band of detector hits belongs to a particular value of V_{S}. At detector coordinate $z' = 0$, corresponding to the spectrometer axis ($z' = \Delta z \cos\theta_{\mathrm{D}}$, Sec. 2.6), the length of the band equals the horizontal source extention, i.e. the spectrometer is double-focusing for this case. For other values of V_{S} the length of the bands becomes larger but the bands remain within the sensitive area of the detector. It is important to note that the bands are always straight and that their width is constant. Hence a one-dimensional position measurement along z' is sufficient for optimal resolution.

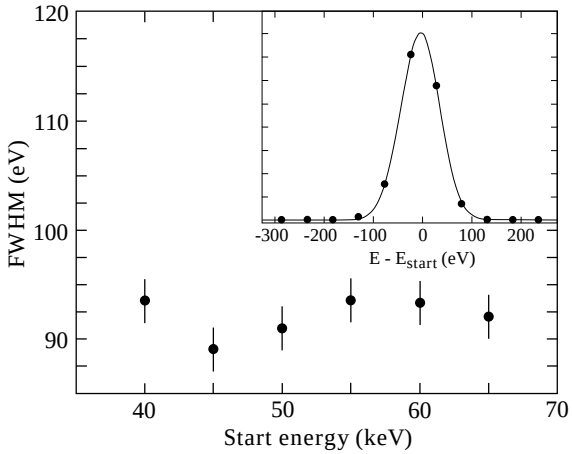

Fig. 13. Computed width of the spectrometer resolution as a function of energy for the setting $E_{\mathrm{mag}} = 71.5\,\mathrm{keV}$. The inset shows the computed resolution function (points) fitted with a gaussian.

The optical properties of the spectrometer can be determined by simulating a measurement with a monoenergetic source. The spectrometer magnet is set to a constant nominal energy $E = E_{\mathrm{mag}}$ and the source voltage V_{S} is varied in equal steps such that the electron beam moves across the whole detector. Using Eq. (8) the step size of V_{S} is chosen such that the centre of the electron distribution on the detector moves by exactly one strip for each step. Each electron, detected at position z', is assigned an energy

$$E = E_{\mathrm{mag}} - e|V_{\mathrm{S}}| + z' D_E \cos\theta_{\mathrm{D}} \,. \tag{10}$$

Because of the chosen step size of V_{S}, the data of the complete detector can easily be combined into one spectrum by simple addition.

The result of a simulation for $E_{\mathrm{mag}} = 71.5\,\mathrm{keV}$ is show in Fig. 13. Plotted is the width of the energy resolution for assumed energies at the source in the range 40 to 65 keV. Within statistical uncertainties, the width is independent of the energy with an average value $\delta E = 92.1 \pm 0.9\,\mathrm{eV}$ FWHM. The given resolution includes the finite width of the source strips (1 mm) and the width of the detector strips (1.27 mm). The inset shows the resolution function for one particular energy. Because of the relatively coarse position resolution of the detector, only few data points are on the line. Nevertheless, the resolution is well fitted by a gaussian. It should be noted that the energy band simultaneously measured is 5.2 keV wide in this case, i.e. 57 times larger than the width of the resolution.

The performance of the spectrometer is conveniently represented by the relative momentum resolution. From the result above we have

$$\delta p/p = 6.9 \times 10^{-4} \quad \text{(FWHM)} \tag{11}$$

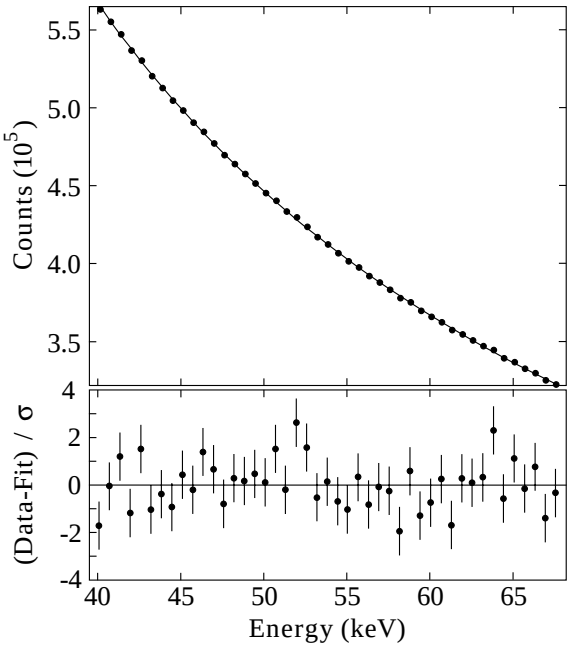

Fig. 14. Computed solid angle correction (points) for the setting $E_{\mathrm{mag}} = 71.5\,\mathrm{keV}$ and best fit using Eq. (5). The lower part shows the difference between data and fit, normalized with the standard deviation.

which is of course independent of E_{mag}. As illustrated by the example above, it is also constant for not too large acceleration voltages, i.e. $e|V_{\mathrm{S}}| \leq E_{\mathrm{mag}}/2$ approximately.

The solid angle correction (Sec. 2.4) can be computed assuming a source which emits a spectrum constant in energy. The result of a simulation for $E_{\mathrm{mag}} = 71.5\,\mathrm{keV}$ is shown in Fig. 14. The data are well represented by a fit using the formula for the solid angle correction (Eq. (5)), augmented with a normalization constant for the arbitrary number of simulated events. The fitted opening angle, $\varphi = 18.5^\circ \pm 1.2^\circ$, is determined by the spectrometer geometry.

For acceleration voltages significantly larger than used to obtain Fig. 14, simulations indicate that the solid angle correction increases more steeply than can be accounted for by Eq. (5). The effect is small and barely recognizable within the statistical uncertainty of the presently available simulations. A likely cause is the blocking of trajectories by the current conductors. An accurate study by Monte Carlo simulation would be very time consuming and it is thus necessary to restrict the range of V_{S} by the condition $e|V_{\mathrm{S}}| \leq 0.4 \cdot E_{\mathrm{mag}}$ for measurements with highest precision.

We have shown in a previous experiment that the optical properties of a Tret'yakov spectrometer can be accurately predicted [11]. As the precise shape of the resolution function is quite uncritical for the present purpose, an extensive (and difficult) experimental investigation was considered unnecessary.

The energy dispersion was measured with accelerated photoelectrons (see next section). The relative difference between experiment and prediction was found to be $(7 \pm 3) \times 10^{-3}$ which is considered negligible.

The source gradient was tested by photoelectrons accelerated from a dummy source but with the dimensions of an actual source. The experiment showed that it is indeed possible to focus a 20 mm wide source on a narrow band on the detector with approximately 2 mm width. It is not possible to measure the resolution function in this way because only a small part of the phase space of a real source is occupied. The experiment showed however that the resolution is not significantly compromised by effects which are neglected in the simulations. These are mainly the deformation of the electric field configuration by the gradient voltage, stray electric fields due to the voltage drop along the current conductors, incomplete compensation of the earth's magnetic field, and in general mechanical deviations from the ideal geometry.

The experimentally determined calibration constant, relating current to momentum, agreed with the prediction to within 4×10^{-4}. The small discrepancy can be accounted for by uncertainties in the radial position of the current conductors and the axial positions of source and detector which are all at the 0.1 mm level.

4 Scattering in the spectrometer

A complete experimental investigation of scattering would require the measurement of the scattering probability for a range of initial energies and all possible detection energies, i.e. a two-dimensional distribution. This was regarded as unnecessary and also would not be readily feasible for the required energies because of the high voltages involved. Instead an experiment was designed with which the reliability of Monte Carlo simulations could be tested.

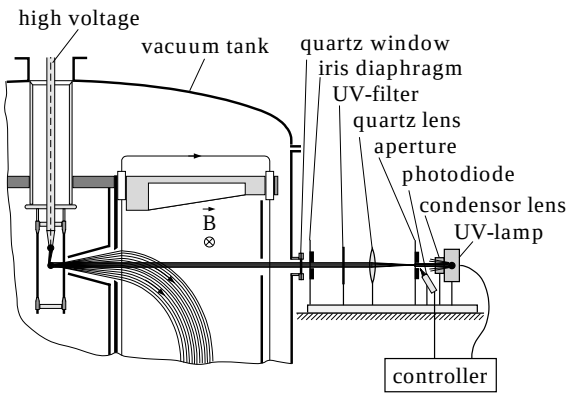

Fig. 15. Optical arrangement to accelerate photoelectrons.

4.1 Measurements

The experimental setup is shown in Fig. 15. A gold-plated sphere (diameter 20 mm) was brought at the nominal source position and put on negative high voltage. The front side of the sphere was illuminated by an homogeneous beam of UV-light. Photoelectrons were accelerated towards the grid and analysed by the spectrometer.

The light beam was produced by a mercury lamp (Osram Hg-100) and quartz optics. Part of the light before the first aperture (diameter 0.3 mm) was reflected onto a photo-diode. The diode signal was used to control the supply current of the lamp to keep the light intensity constant.

A UV filter (type UG11) was inserted into the light beam, cutting off light with wavelengths below approximately 275 nm. This was convenient because otherwise the large optical dispersion of quartz in the UV region makes it difficult to form a parallel beam. Effectively, only a narrow wavelength band was used, limited by the filter and the work function of the sphere.

Within the solid angle accepted by the spectrometer, the sphere closely simulates an isotropic source on a small spot at the centre of the sphere. This is easily seen by noting that a large part of the acceleration occurs close to the sphere where the electric field points in radial direction.

The computation of trajectories was performed using the electric field of a conducting sphere between two infinite grounded planes replacing the grid. The diameter of the effective source spot was found to be 2 mm. Experimentally, the small spot size was verified by simply observing the distribution of electron positions on the detector.

Measurements were performed with various spectrometer settings and with acceleration voltages in the range from 30 to 60 kV. Here we discuss only the

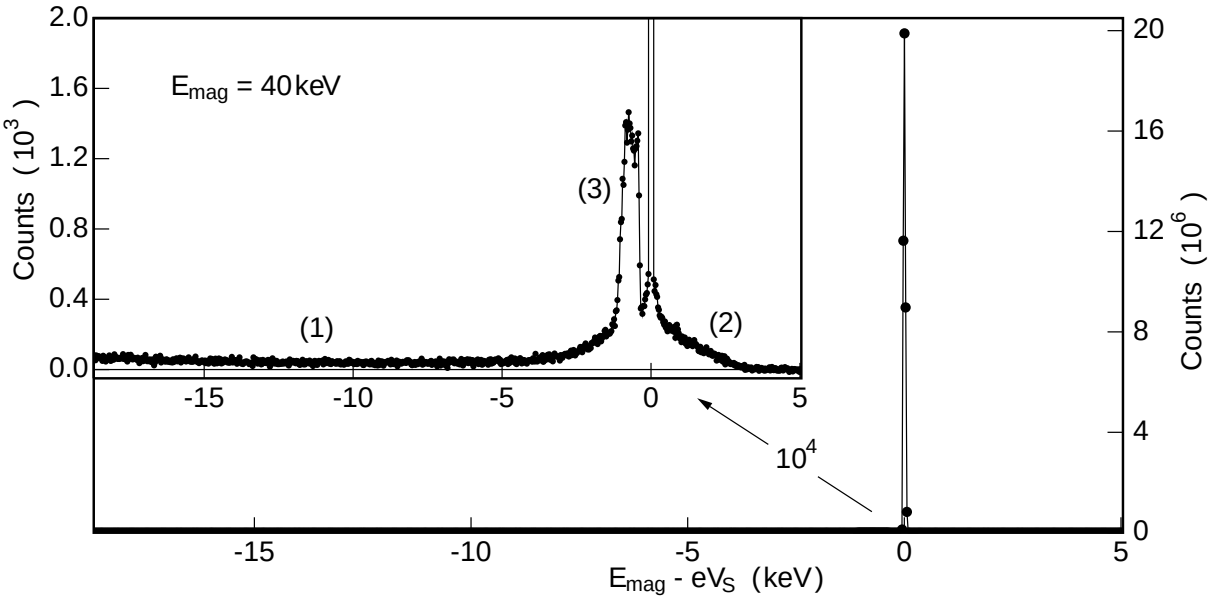

Fig. 16. Measured energy distribution of scattered electrons for $E_{\mathrm{mag}} = 40\,\mathrm{keV}$. The bin width is 29 eV. The inset shows the same data but with the vertical scale expanded by a factor 10^4.

results with the setting $E_{\mathrm{mag}} = 40\,\mathrm{keV}$. Results with other settings are quite similar.

For the following discussion, it is important to distinguish clearly between various electron energies. These are the energy after acceleration ($e|V_{\mathrm{S}}|$), the energy assigned to a detected electron using the position information of the detector and Eq. (10), and finally the energy deposited in the detector and determined from the measured pulse height.

A typical scattering spectrum is shown in Fig. 16. The energy of detected electrons was computed using Eq. (10), which is nominally the energy before acceleration. The spectrum is dominated by an huge peak of unscattered electrons at zero energy (actual energy around 40 keV). The distribution of scattered events can be seen in the inset which shows the same spectrum but with the vertical scale expanded by a factor 10000. Three distinct features can be recognized: A flat tail (1) corresponding to electrons which have lost energy after acceleration, a somewhat asymmetric bump (2) centred at the main peak, and a side peak (3). Actually this peak is an artifact of the measurement and the data in the range $-2.0\,\mathrm{keV}$ to $-0.5\,\mathrm{keV}$ must be discarded. The side peak is caused by electrons which are released from the support bare of the sphere by scattered light. Because of the shifted start position these electrons arrive at a shifted position on the detector causing a wrong assignment of energy.

In the statistical average, the events in the tail and the bump can be distinguished by applying cuts to the pulse-height distribution measured by the

Table 1
Measured fraction of events in the tail (1) and the bump (2) for various pulse-height cuts. The statistical errors are of order 1%.

Cut (keV)	Fraction (1) (10^{-4})	Fraction (2) (10^{-4})
20 – 57	9.43	5.84
26 – 57	9.24	3.55
31 – 57	9.09	1.52
37 – 57	9.17	0.72

detector. This is illustrated in Tab. 1. The fraction (1) was computed by summing the events in the energy range $-18.8\,\mathrm{keV}$ to $-2.0\,\mathrm{keV}$ (see Fig. 16) and normalizing by the number of events in the main peak. Similarly, fraction (2) was obtained from the events in the range $0.2\,\mathrm{keV}$ to $8.3\,\mathrm{keV}$.

The fraction (1) of events is nearly independent of the cut. In contrast, the bump fraction decreases strongly with narrower cuts. The interpretation of these observations is straight forward. The electrons in the tail have been accelerated to an energy larger than E_{mag} ($40\,\mathrm{keV}$ in this case). As the cut independence implies that they arrive with an actual energy close to E_{mag} at the detector, they must have lost the difference by scattering and this must have occurred somewhere in the source region so that the spectrometer could still analyse them efficiently after scattering.

The strong cut dependence of the events in the bump implies that these electrons are detected with a broad distribution of their actual energy. Most of these could not have passed through the spectrometer with the energy as determined by pulse height and not being rejected by the spectrometer. Hence, the events in the bump were from electrons which arrived at the detector region with essentially correct energy and were scatted there causing them to be detected at the wrong position. This in turn led to a wrong energy assignment by Eq. (10). This interpretation is compatible with a sharp cut-off (at $3.3\,\mathrm{keV}$ in Fig. 16) of the bump which is precisely given by the size of the detector scaled with the spectrometer dispersion.

The sphere simulates a small source whereas real sources being used are quite extended. For this reason, measurements were made with the sphere shifted from the spectrometer axis by up to $15\,\mathrm{mm}$ (perpendicular to the plane of Fig. 15). The fraction of events in the bump was found to be nearly independent of the sphere position. The tail fraction, however, showed a quite large position dependence, with relative variations up to 25% from the average. This surprising observation is explained by the fact that the transmission probability of electrons from a small source through the inner ring of current conductors, ar-

riving at the detector without scattering, is position dependent. The variation of the tail fraction thus arose because the normalization was made with the number of detected electrons and not with the number of electrons accelerated at the sphere.

All these observations are explained quantitatively by Monte Carlo simulations to be discussed next.

4.2 Monte Carlo simulation

The interaction processes of fast electrons passing through a solid material are conveniently divided in elastic scatterings from ion cores and in inelastic scatterings from electrons with typically small angular changes. Radiative processes are negligible for the energies considered here. Relativistic kinematics was used throughout the simulations.

The elastic differential cross section was taken from the Wentzel model which is the first Born approximation of an exponentially screened Coulomb potential [12]. This is a sufficiently good approximation for our case, i.e. materials with small atomic number Z and energies above about 20 keV. Choosing the screening length to be $R = 0.885 \cdot Z^{-1/3} a_{\mathrm{B}}$ (a_{B} Bohr's radius) comparison with tabulations from detailed calculations [13] gives good agreement for scattering angles larger than about 2°. For smaller angles the deviations become large but for Monte Carlo simulations this should be negligible. In any case a more accurate treatment of small angle scattering would require taking solid state effects into account which is not warranted for our purpose.

The simplest method to take inelastic processes into account is the continuous slowing down approximation (CSDA). At each elastic interaction point, the path length to the previous point is determined and the average energy loss subtracted. This is easy to implement and leads to a fast execution of the simulation. Backscattering from solid objects is well simulated by CSDA and we have used it for spectrometer objects (baffles etc.) for which transmission is impossible. The average energy loss was computed by interpolating tabulated values from Ref. [14].

The CSDA method gives poor results for thin objects, in particular for the energy distribution of transmitted electrons. For such cases (grid wires etc.) we have used a semi-empirical model proposed be Liljequist [15] and extended in Ref. [16]. Energy loss processes are represented by discrete excitations of bound atomic electrons and by elastic scattering from quasi-free electrons at rest. For the latter the Møller cross section was used. The parameters of the model are determined by the Bethe sum rule and the stopping power [14].

Simulations with this model are slow, in particular because many interactions with small energy loss are generated. As these do not contribute strongly to the energy straggling, a hybrid method was adopted as proposed in Ref. [16]. A principally arbitrary cut-off energy E_c is introduced. All interactions with energy loss less than E_c are treated by CSDA, such with larger energy loss by the more detailed model.

The implementation of the scattering algorithm was tested by simulating well known published experimental data. The angular distribution of 20 keV electrons passing through a 1.115 μm aluminium foil [17] seems to be a particular simple case. The experimental data were reproduced at the few percent level even with the CSDA method. Similarly good results with the hybrid method and a small value of E_c were obtained for the energy distribution of electrons with initial energies of 30 or 70 keV, being backscattered from solid aluminium [18,20]. The results with the CSDA method showed noticeable deviations for this case, being as large as 10%. Finally, we mention the energy distribution of 20 keV electrons passing through a 1.04 μm thick foil of aluminium [19]. The CSDA method fails completely for this case. The results with the hybrid method showed good agreement in general, but even with $E_c = 0$ discrepancies remained, being as large as 20%. We note that simulated data, reported in Ref. [20] for the same experiment, show approximately the same deviations, although much more refined cross sections were used by these authors.

The complete simulation of the spectrometer including scattering requires a large amount of computing time. One reason is that the probability of an electron being scattered and detected is small. As a consequence, a large number of trajectories through the spectrometer must be computed to obtain a statistically satisfactory sample of scattered events. The efficiency was improved in the following way. A certain number $N_m \geq 1$ is defined. Each electron hitting a scattering object is replaced by N_m electrons with identical kinematic variables at the object surface and their paths through the material are followed using statistically independent random numbers. The trajectories of those electrons leaving the object are then computed as usual and the number of detected electrons is normalized with N_m.

This procedure can be justified by noting that the path through a material resembles a random walk. Hence, the velocity of electrons leaving an object is only weakly correlated with the direction of the initial velocity. Moreover, the fraction of electrons leaving a thick object is small and the fraction of those being detected is smaller still.

A reasonable choice for N_m was found to be in the range 25 to 50. Not much is gained with larger values as the computation of scattering becomes dominant. The presence of statistical artifacts was tested by making N_m much larger than what would be useful. No deviations from usual Poisson statistics were

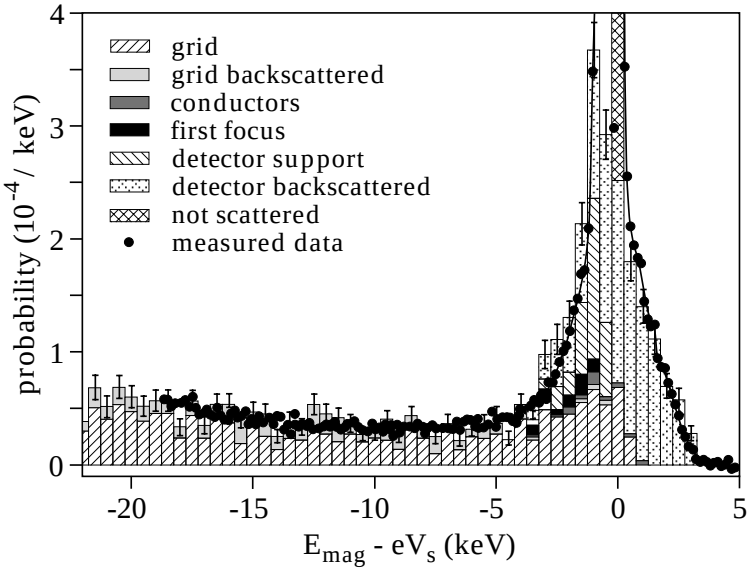

Fig. 17. Comparison of the measured and the computed energy distribution of scattered electrons.

observed with values as large as $N_m = 250$.

4.3 Comparing experiment and simulation

All experimental data (Sec. 4.1) are quantitatively reproduced by the simulations. The systematic deviations are typically smaller than 15%. No parameter of the simulation was adjusted to the experimental data.

An example of a simulated scattering spectrum is shown in Fig. 17 and compared with the experimental data already displayed in Fig. 16. The contributions from the various objects are indicated by different shades. The tail is dominated by electrons scattered from the grid wires. Electrons, scattered from the current conductors also contribute to the tail but with a much smaller fraction. Hence the measures taken to reduce scattering from the conductors (Fig. 2) are quite effective.

The bump is caused by electrons which are backscattered from the detector or its support structures (see Fig. 8). Various event types may be envisioned but only two are of importance. The first type corresponds to electrons which hit the support directly and are then scattered into the detector. The second type involves two scatterings. An electron is backscattered from the detector (silicon), hits the support and from there is scattered into the detector again. Thus in both types, an electron arrives at the detector with the correct energy but a wrong energy is assigned because the detector determined a wrong position (see Eq. (10)). Clearly, the error in the assigned energy can be as large as

the size of the detector scaled with the spectrometer dispersion, but definitely not larger. This explains the sharp cut-off observed at higher energy (3.3 keV in Fig. 17).

The distribution of energy deposited in the detector by an electron being backscattered is very broad. Hence, the number of events in the bump can be strongly suppressed by narrowing the pulse-height cut, in good agreement with the experiment.

5 Conclusion

We have presented a β–spectrometer suitable for high precision measurements. High count rate and at the same time good energy resolution is achieved by the use of a large size detector with position resolution and an electrostatically compensated extended source. Dead-time losses are nevertheless small and easily correctable as the electronics provides seperate channels for all detector strips.

The use of an extended source is essential as this is the only way to have a strong but very thin source. Energy loss in the source layer is notoriously difficult to correct in a measured β–spectrum and β–spectroscopy has always been plagued by sources being too thick for a certain purpose.

The capability of the spectrometer can be illustrated by comparing with an assumed reference instrument having the same energy resolution but uses only a small source and a detector without position measurement. Obtaining the equivalence would require the use of 20 sources each being measured simultaneously by 96 spectrometers. The gain in rate achieved with respect to the reference is thus a factor $20 \times 96 = 1920$.

The combination of a magnetic spectrometer with electrostatic scanning of the energy has been widely used in recent tritium experiments. We have extended this method to much higher energies. The implied high voltages can be handled, up to a certain value, and we have the benefit that measured β–spectra are independent of an energy-dependent detection efficiency which would otherwise be difficult to correct.

Finally, scattering in the spectrometer is another source of systematic uncertainties. We have demonstrated that with today's computers it is possible, also for complex geometries and at relatively small energies, to accurately predict scattering probabilities by Monte Carlo methods. Thus all essential ingredients are at hand for the purpose discussed in the introduction.

Acknowledgements

This work has been supported by the Swiss Science Foundation and by the Paul Scherrer Institute (PSI) which is gratefully acknowledged. The mechanical work for the spectrometer has been performed to great perfection at our institute's machine shop and we thank all members very much. The silicon detector has been designed by Roland Horisberger (PSI). We thank him very much and appreciate the close collaboration and many helpful hints. The detector electronics was designed and built at the electronic shops of our institute and of PSI which we gratefully acknowledge.

References

[1] R.E. Shrock, Phys. Lett. B 96 (1980) 159.

[2] R.G.H. Robertson et al., Phys. Rev. Lett. 67 (1991) 957.

[3] E. Holzschuh, M. Fritschi, and W. Kündig, Phys. Lett. B 287 (1992) 381.

[4] Ch. Weinheimer et al., Phys. Lett. B 300 (1993) 210.

[5] W. Stoeffl and D.J. Decman, Phys. Rev. Lett. 75 (1995) 3237.

[6] A.I. Belesev et al., Phys. Lett. B 350 (1995) 263.

[7] F.E. Wietfeldt and E.B. Norman, Phys. Rep. 273 (1996) 149.

[8] G. Gelmini and E. Roulet, Rep. Prog. Phys. 58 (1995) 1207.

[9] E.F. Tret'yakov, Izv. Akad. Nauk SSSR, Ser. Fiz. 39 (1975) 583, (Engl. trans. Bull. USSR Acad. Sci. Phys. Ser. 39 (1975) 102).

[10] H.T. Lau, Numerical Library in C for Scientists and Engineers (CRC Press, Florida, 1995).

[11] M. Fritschi, E. Holzschuh, W. Kündig, and H. Stüssi, Nucl. Phys. B (Proc. Suppl.) 19 (1991) 205.

[12] S.E. Schnatterly, Solid State Physics 34 (1979) 275.

[13] W.E. Riley, At. Data and Nucl. Data Tab. 15 (1975) 444.

[14] N.J. Berger and S.M. Seltzer, ICRU Report 37 (1984).

[15] D. Liljequist, J. Phys. D 16 (1983) 1587.

[16] F. Salvat and J.M. Fernández-Varea, Nucl. Inst. and Meth. B 63 (1992) 255.

[17] R.N. Thomas, Ph.D. Thesis (Cambridge University 1969).

[18] Darlington, J. Phy. D 8 (1975) 85.

[19] R. Shimizu et al., J. Phys. D 9 (1976) 101.

[20] J.M. Fernández-Varea et al., Nucl. Inst. and Meth. B 108 (1996) 35.